Dynamic Material Response of Aluminum Single Crystal Under Microscale Laser Shock Peening

Sinisa Vukelic
Youneng Wang
Jeffrey W. Kysar
Y. Lawrence Yao

Department of Mechanical Engineering,
Columbia University,
New York, NY 10027

The process of laser shock peening induces compressive residual stresses in a material to improve material fatigue life. For micron sized laser beams, the size of the laser-target interaction zone is of the same order of magnitude as the target material grains, and thus the target material must be considered as being anisotropic and inhomogeneous. Single crystals are chosen to study the effects of the anisotropic mechanical properties. It is also of interest to investigate the response of symmetric and asymmetric slip systems with respect to the shocked surface. In the present study, numerical and experimental aspects of laser shock peening on two different crystal surfaces (110) and (1$\bar{1}$4) of aluminum single crystals are studied. Lattice rotations on the top surface and cross section are measured using electron backscatter diffraction, while residual stress is characterized using X-ray microdiffraction. A numerical model has been developed that takes into account anisotropy as well as inertial terms to predict the size and nature of the deformation and residual stresses. Obtained results were compared with the experimental finding for validation purpose. [DOI: 10.1115/1.3106034]

1 Introduction

It is well known that the process of shot peening is beneficial for the improvement of fatigue behavior of treated parts. The process consists of bombarding a surface with hard particles, which induce compressive stresses in the surface by repeated impacts. The process of laser shock peening (LSP) was introduced in the second half of the 20th century [1–3]. It is a surface treatment wherein laser induced shocks introduce compressive residual stress of the same order of magnitude as conventional shoot peening but much deeper into the material, resulting in an improvement in performance under cyclic loading of various materials, such as copper, aluminum, nickel, etc. [4]. LSP is much easier to control than conventional shot peening allowing treatment of only selected regions by precisely determining the position of the laser. Another benefit is that LSP induces little or no apparent change to the surface finish. However, this technique has not been widely used in the industry because of the expense of high power lasers needed to induce beam spot sizes of the order of millimeters necessary in order to treat large areas.

The recent development in micro-electromechanical systems (MEMS) devices has raised the issue of improvement of reliability of components of those systems by using *microscale* LSP (μLSP). In particular, μLSP can improve the fatigue life and wear resistance of those components by altering residual stress distribution with a spatial resolution of several microns. In this process, the specimen is coated with aluminum foil or black paint, which acts as an ablative layer. As a consequence, the material to be treated is not subjected to high temperatures, so that residual stresses are induced only by shock pressure. Thus no thermally-induced microstructure change is induced. Much work in this field has been performed on polycrystalline materials [5]. However, in μLSP the beam spot size is several microns and the average grain size in polycrystalline aluminum and copper is about same of order of magnitude, which means that in most cases only a few grains, at most, are affected by a single laser pulse. Therefore the material properties must be considered as anisotropic and heterogeneous. This has motivated a prior study of the response of single crystals of aluminum and copper subjected to laser shock processing in order to better understand the effects of anisotropy [6,7]. Residual stresses were characterized using X-ray microdiffraction with the method introduced by Ungar et al. [8]. A numerical model was established and the results compared with the experiment for two different orientations of aluminum and copper single crystals.

It is well known that single crystals exhibit anisotropic plastic properties. One of the early efforts to predict the behavior of anisotropic plastic media was by Hill [9] who generalized the circular yield surface employed in classical slip line theory by Hencky [10] and Prandtl [11] to an elliptical yield surface. Rice [12] and Booker and Davis [13] further generalized slip line theory to be applicable to arbitrary anisotropy. Rice [12] applied the theory to a punch impinging onto the surface of an anisotropic plastic medium. Also Rice [14], and later Drugan [15] derived asymptotic crack tip stress field solutions for elastic ideally-plastic single crystals. Also Kysar and co-workers [16,17] employed anisotropic slip line theory to find the analytical solution for the stress distribution and deformation state around a cylindrical void in a single crystal.

Anisotropic slip line theory has also been used to investigate the effect of laser shock peening of single crystals. Wang et al. [18], estimated the size of the deformed region due to laser shock peening on an aluminum single crystal of a nonsymmetric (1$\bar{1}$4) orientation assuming a Gaussian pressure distribution from the laser shock, albeit while neglecting inertial terms in the governing equations. The approximate analytical solution has been augmented with a finite element numerical analysis. The analysis of the Al single crystal of (1$\bar{1}$4) orientation is interesting because there is only one slip system predicted to be active directly under the applied pressure. It is of interest to also investigate a more symmetric orientation, which activates multiple slip systems under the Gaussian pressure distribution. In the present study, the (110) orientation is chosen because of its symmetry. Another motivation for the work presented herein is the fact that real applications may involve textured polycrystalline material in which the orientation of grains has predominantly low Miller indices.

Thus, the objective of this work is the study of aluminum single crystal behavior under Gaussian pressure distribution induced by

Contributed by the Manufacturing Engineering Division of ASME for publication in the JOURNAL OF MANUFACTURING SCIENCE AND ENGINEERING. Manuscript received July 22, 2008; final manuscript received January 19, 2009; published online May 29, 2009. Review conducted by Bin Wei.

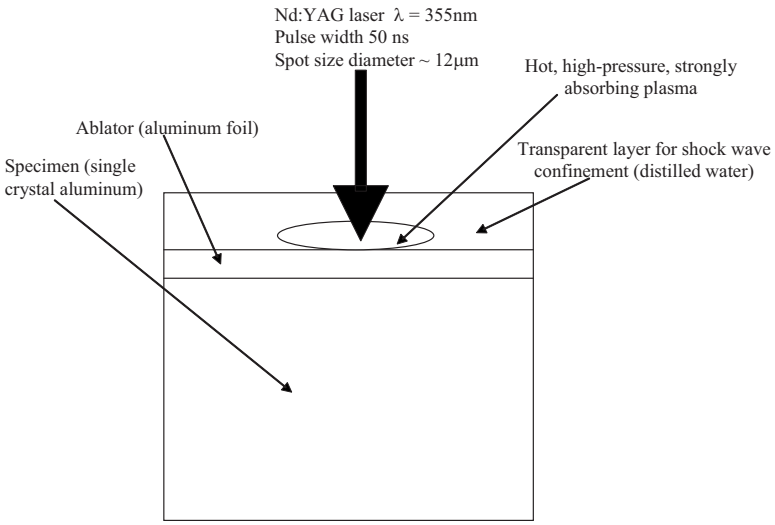

Fig. 1 Experimental setup

μLSP for two different crystallographic orientations: one nonsymmetric with high Miller index $(1\bar{1}4)$, and the other symmetric with low Miller index (110). The deformation state is characterized experimentally. In addition, the finite element method (FEM) is used for a detailed analysis of single crystal material response to dynamic loading to complement the study for the case where the inertial terms are included.

2 Laser Shock Processing

Under the radiation of an intense laser pulse, an ablative surface layer deposited on a metal target is rapidly transformed into plasma, characterized by high pressure (1–10 GPa) and high temperature. As the plasma expands, shock waves propagate into the target. It should be noted that there is a significant difference in magnitude of the pressure wave depending on whether the expanding plasma is confined or not. If unconfined, i.e., open air conditions, the pressure can reach a peak value of only several hundred MPa. On the other hand, if confined by water or some other medium, studies have shown [19] that the shock pressure rises five times or more in comparison to the open air condition, with a shock pressure duration two to three times longer than the laser pulse itself. These pressures are far above the yield stress of most materials, thus it is very likely that plastic deformation will occur resulting in a compressive residual stress distribution [1] on the treated surface of the material

For the case of laser shock processing, the target material is usually coated with an ablative layer of metallic foil, paint, or adhesives in order to prevent elevated temperatures from reaching the target. Thus, the shock process can be approximated as adiabatic; only the mechanical effects of pressure need to be taken into account in an analysis.

3 Experimental Setup and Characterization

An aluminum single crystal is used in this study. The sample is mounted on a three circle goniometer and its orientation is determined by Laue diffraction (Cu-K_α X-ray source). The specimen is cut to size with a wire electrical discharge machine (EDM) and the resulting heat affected zone (HAZ) is removed via mechanical polishing. Finally, electropolishing is used in order to remove any residually deformed material. Laser shock peening is then applied along a line on the specimen surface. The shocked surface is then characterized with various methods, after which the crystal is sectioned with wire EDM and the cross-sectional surface is again mechanically polished and electropolished in order to examine the plastic deformation, which occurs on the cross section.

A frequency tripled Q-switched Nd:YAG laser with wavelength $\lambda = 355$ nm in TEM_{00} mode is used for the μLSP experiments with a beam diameter of 12 μm pulse duration of 50 ns and laser intensity of about 4 GW/cm^2. A 16 μm thick polycrystalline aluminum foil is used as an ablative coating applied tightly over an evenly spread layer (10 μm thick) of high vacuum grease. The specimen is put into a shallow container filled with distilled water to about 2 mm above the sample's top surface, as shown in Fig. 1. More details about laser shocking can be found at Refs. [5,7]. In order to obtain an approximate 2D deformation state, shocks are applied with a 25 μm spacing along the $[1\bar{1}0]$ direction as discussed in Ref. [7] and illustrated in Fig. 2. Detailed discussion about the formation of the approximate two-dimensional deformation can be found in Refs. [14,16,17]. Crone et al. [20] summarized the geometrical conditions that need to be met in order to achieve plane strain conditions.

μLSP induces rotation of the crystal lattice as a consequence of plastic deformation into the single crystal, which can be characterized experimentally by comparing the as-deformed crystallographic orientation [17,18] relative to the known undeformed state. Lattice orientation is measured using electron backscatter diffraction (EBSD) with micrometer scale spatial resolution.

In the work presented here, the shocked surface is scanned via EBSD first, which provides information about lattice rotation on the treated surface. In order to obtain information about the depth of the affected region and the magnitude of lattice rotation under the surface, EBSD mapping is also employed on a cross section of the sample.

For these measurements an HKL Technology system attached to a JEOL JSM 5600LV scanning electron microscope (SEM) is

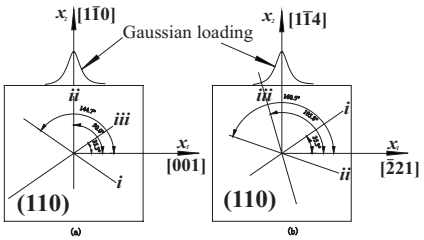

Fig. 2 Plane strain slip systems corresponding to (*a*) (110) orientation and (*b*) $(1\bar{1}4)$ orientation; effective in-plane slip systems are labeled as *i*, *ii*, and *iii*

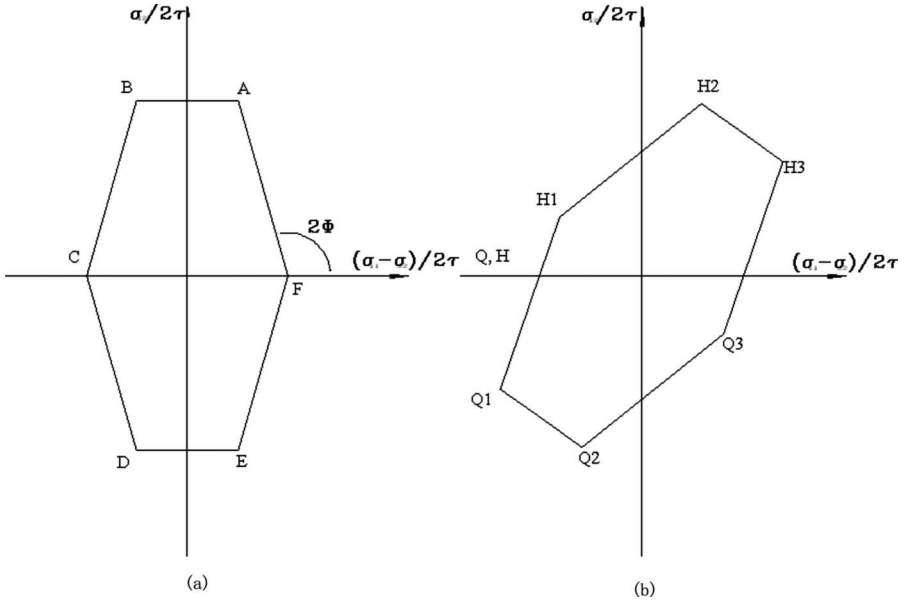

Fig. 3 Yield locus for (*a*) (110) orientation and (*b*) (1$\bar{1}$4) orientation

used with a scan area of 200×200 μm^2 and 120×120 μm^2 on the shocked surface and cross section, respectively, with 3 μm step size.

X-ray microdiffraction is used to characterize residual stress near the shock line. Synchrotron radiation as a source of X-ray beams is employed because of its high resolution and high intensity. The beam is focused using a glass capillary such that a spatial resolution of several microns can be achieved. Beamline X20A at the National Synchrotron Light Source (NSLS) at Brookhaven National Laboratory is used for the diffraction measurements with monochromatic synchrotron radiation at 8.0 keV. A Huber two-circle vertical diffractometer with partial chi (χ) and phi (ϕ) arcs is employed for diffraction. Measurements are conducted along a line perpendicular to the shock line with 10 μm spacing and acquired with modified version of SPEC software package [21]. The measured X-ray profile is processed using the method of Ungar et al. [8]. More details about measurement techniques can be found at Ref. [7].

4 Numerical Simulation Conditions of Single Crystals

4.1 Problem Formulation. Material response under dynamic loading has been studied as shock wave propagation in isotropic materials under LSP [22,23]. Anisotropy is studied in Ref. [24] who formulated analytic solution for plane wave propagation in anisotropic elastic-plastic solids. Single crystal plasticity was combined with dynamic loading by Nemat-Nasser et al. [25] through the study of dynamic void collapse. In this study a model has been developed to simulate single crystal material response to the dynamic Gaussian pressure loading found in μLSP process under plane strain conditions.

The analysis is performed with the commercial FEM program ABAQUS/STANDARD with user defined material subroutine (UMAT), based on the single crystal plasticity theory formulated by Asaro [26], written by Huang [27] and modified by Kysar [28]. The mesh consists of two-dimensional eight-noded quadrilateral elements with reduced integration. The crystallographic orientation relative to the finite element mesh is chosen such that plane strain is achieved [6,18]. Pressure applied on two different surfaces (110) and the (1$\bar{1}$4) are simulated. They correspond to the symmetric and asymmetric yield loci, respectively, as seen in the Fig. 3. Boundaries are modeled with semi-infinite elements, and therefore there are no reflections of the elastic waves once they propagate through the domain of interest. The loading Gaussian spatial distribution pressure is as follows:

$$p(x) = p_0 \exp\left(-\frac{x^2}{2R^2}\right) \tag{1}$$

In addition a temporal aspect is added to the pressure. Peyre et al. [23] measured the temporal pressure profile of pulses with 3 ns and 10 ns durations using the VISAR technique. They reported that as the duration of laser pulse increases the peak pressure value decreases and full-width-at-half-maximum (FWHM) increases. Following this formulation, the temporal profile is generated as a semifree parameter to match the experimental findings of displacement and lattice rotation. The temporal pressure profile is shown in Fig. 4. In addition, in order to accommodate the lateral growth of plasma, its radius is set to be three times larger than the radius of the laser spot. The initial yield stress is set to be 300 MPa and saturation stress 600 MPa, values that appear to be reasonable, following Refs. [23,25].

4.2 Constitutive Relationships. The dynamic loading and wave propagation is characterized using the formulation based on the dynamic principle of virtual work (e.g., Refs. [29,30]):

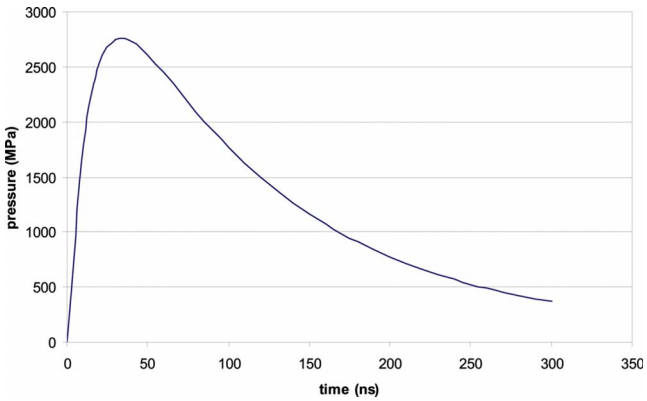

Fig. 4 Temporal pressure distribution during the loading in the numerical simulation

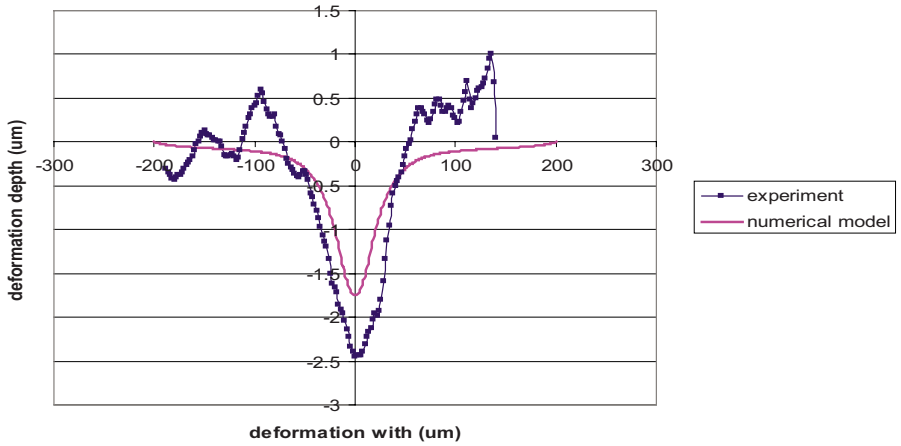

(a)

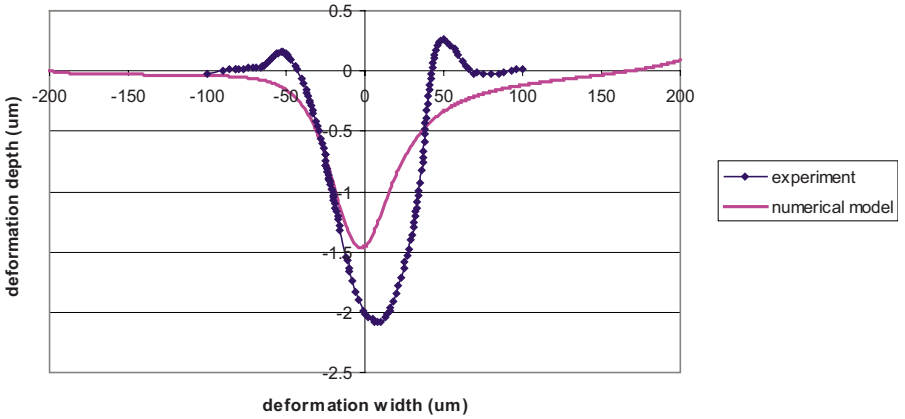

(b)

Fig. 5 Deformation field measured via profilometer and AFM, respectively: (*a*) orientation (110), and (*b*) orientation (1$\bar{1}$4)

$$\int_V \bar{\tau}:\delta\bar{\varepsilon}dV = \int_S \boldsymbol{t}\delta\boldsymbol{v}dV - \int_V \rho\frac{\partial^2\boldsymbol{u}}{\partial t^2}\delta v dV \tag{2}$$

where τ and ε are any conjugate pair of stress and strain, $\boldsymbol{u}$ represents displacement, and $\boldsymbol{t}$ is surface traction. At the end of each solution increment the main program passes the UMAT the following variables: time increment, stress state, strain increment, and solution dependent state variables($s_i^{(\alpha)}$, $n_i^{(\alpha)}$, $\gamma^{(\alpha)}$, $g^{(\alpha)}$, etc.) defined by the user. The UMAT updates the stress state and solution dependent variables and calculates the material Jacobian matrix ($\partial\sigma_{ij}/\partial\varepsilon_{kl}$) based on Eqs. (3)–(11) below. These new values are then returned to the solver where the new stress state is applied as a load increment and calculates the corresponding strain increment. This process is repeated until the job is complete.

When loading of an elastic-plastic crystal takes place, total strain rate is given as a sum of its elastic and plastic components, assuming an infinitesimal deformation gradient tensor as follows:

$$\dot{\varepsilon}_{ij} = \dot{\varepsilon}^e + \dot{\varepsilon}^p \tag{3}$$

According to Schmid [31], plastic slip occurs when the shear stress resolved on the crystallographic plane in the slip direction reaches some critical value. The Schmid factor is defined as

$$\mu_{ij}^{(\alpha)} = \tfrac{1}{2}(s_i^{(\alpha)}n_j^{(\alpha)} + s_j^{(\alpha)}n_i^{(\alpha)}) \tag{4}$$

where $s_i^{(\alpha)}$ and $n_i^{(\alpha)}$ are vectors that define slip directions and slip normals on the αth slip system, respectively. The Schmid factor is used to calculate the resolved shear stress $\tau^{(\alpha)}$ and the plastic strain rate on each particular slip system as follows:

$$\tau^{(\alpha)} = \sigma_{ij}\mu_{ij}^{(\alpha)} \tag{5}$$

$$\dot{\varepsilon}_{ij}^p = \sum_{\alpha=1}^{N} \mu_{ij}^{(\alpha)}\dot{\gamma}^{(\alpha)} \tag{6}$$

where σ_{ij} is the stress tensor, $\dot{\gamma}^{(\alpha)}$ is the engineering shear strain on the αth slip system, and summation is done over all N slip systems.

The magnitude of the plastic strain increment is determined using the following rate dependent power-law formulation introduced by Hutchinson [32]:

$$\dot{\gamma}^{(\alpha)} = \dot{\gamma}_0^{(\alpha)}\ \mathrm{sgn}(\tau^{\alpha})\left|\frac{\tau^{(\alpha)}}{g^{(\alpha)}}\right|^m \tag{7}$$

where $\dot{\gamma}_0^{(\alpha)}$ is reference strain rate, with reference stain rate set to be 0.001 s^{-1} in this model, and $g^{(\alpha)}$ is the strength of the αth slip system. With this formulation, significant slip occurs only on

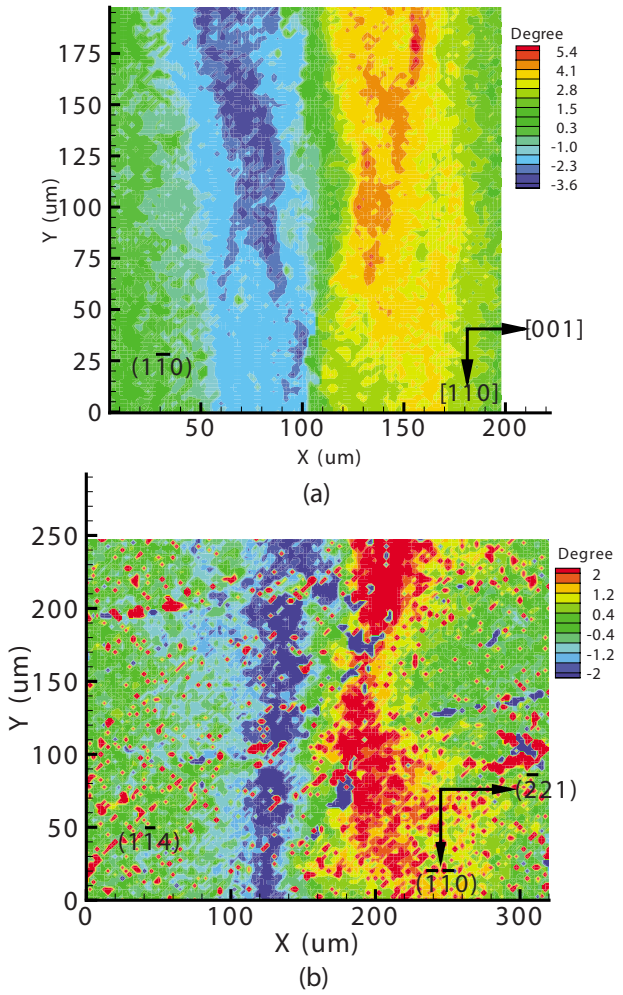

Fig. 6 Lattice rotation contour map on a sample surface; (*a*) (110) rotation, and (*b*) (1$\bar{1}$4) rotation

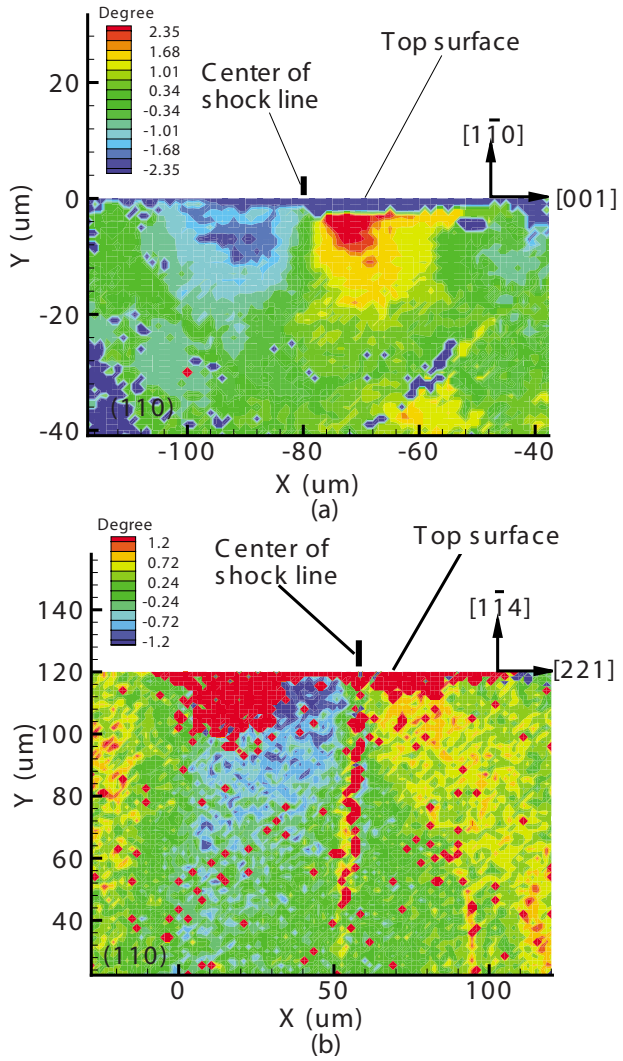

Fig. 7 Lattice rotation contour map on the (110) cross section; positive rotation is counterclockwise about the *z*-axis

those systems for which $\tau^{(\alpha)} \cong g^{(\alpha)}$. Moreover, a large value of exponent m ($m=50$) makes this formulation practically rate independent and $g^{(\alpha)}$ becomes essentially the critical resolved shear stress on the given slip system.

Hardening of the material is characterized through the evolution of the strength $g^{(\alpha)}$ of each slip system. With increasing plastic deformation $g^{(\alpha)}$ evolves as a function of hardening moduli $h_{\alpha\beta}$, which can be decomposed into self-hardening ($\alpha=\beta$) and latent-hardening ($\alpha \neq \beta$) moduli, and shear strain rate.

$$g^{(\alpha)} = \sum_{\beta=1}^{N} h_{\alpha\beta}\dot{\gamma}^{(\beta)} \tag{8}$$

Several hardening models have been proposed by Bassani and Wu [33] Cuitino and Oritz [34] and others to characterize $h_{\alpha\beta}$. In this study the Pierce, Asaro, and Needleman (PAN) [35] model is used to simulate hardening.

$$h_{\alpha\alpha} = h(\gamma) = h_0 \sec h^2 \left| \frac{h_0 \gamma}{\tau_s - \tau_0} \right| \tag{9}$$

$$h_{\alpha\beta} = qh(\gamma), \quad (\alpha \neq \beta) \tag{10}$$

where h_0 is the initial hardening modulus, τ_0 is the initial value of the hardening modulus, τ_s is saturation stress of the hardening moduli, and q is the ratio between the latent-hardening rate and self-hardening rate of a particular slip system.

The stress rate associated with the elastic strain rate can be formulated as

$$\dot{\sigma}_{ij} = L_{ijkl}\dot{\varepsilon}^e_{kl} = L_{ijkl}(\dot{\varepsilon}_{kl} - \dot{\varepsilon}^p_{kl}) \tag{11}$$

where L_{ijkl} is the elastic moduli tensor.

5 Results and Discussion

5.1 Deformation Measurements and Comparison With Simulation Results. Deformation measured via optical profilometer and atomic force microscope (AFM) superimposed with numerical results for comparison is shown in Fig. 5. Measurements are taken at several different locations along the shocked line and displacements appear to be quite uniform suggesting approximate two-dimensional deformation state. As seen in Fig. 5 the width of deformation is about 180 μm and 130 μm for samples with orientations (110) and (1$\bar{1}$4), respectively, and the depth of deformation is between 2 μm and 2.5 μm. It should be noted that the numerical model underestimates the depth of the deformation for about 30%, which is due to the assumptions made in the modeling. Deformation is larger in the (110) case than in the (1$\bar{1}$4) and that is due to the fact that former orientation corresponds to the double slip, two slip systems are active under Gaussian pressure distribution, whereas the latter is the single slip

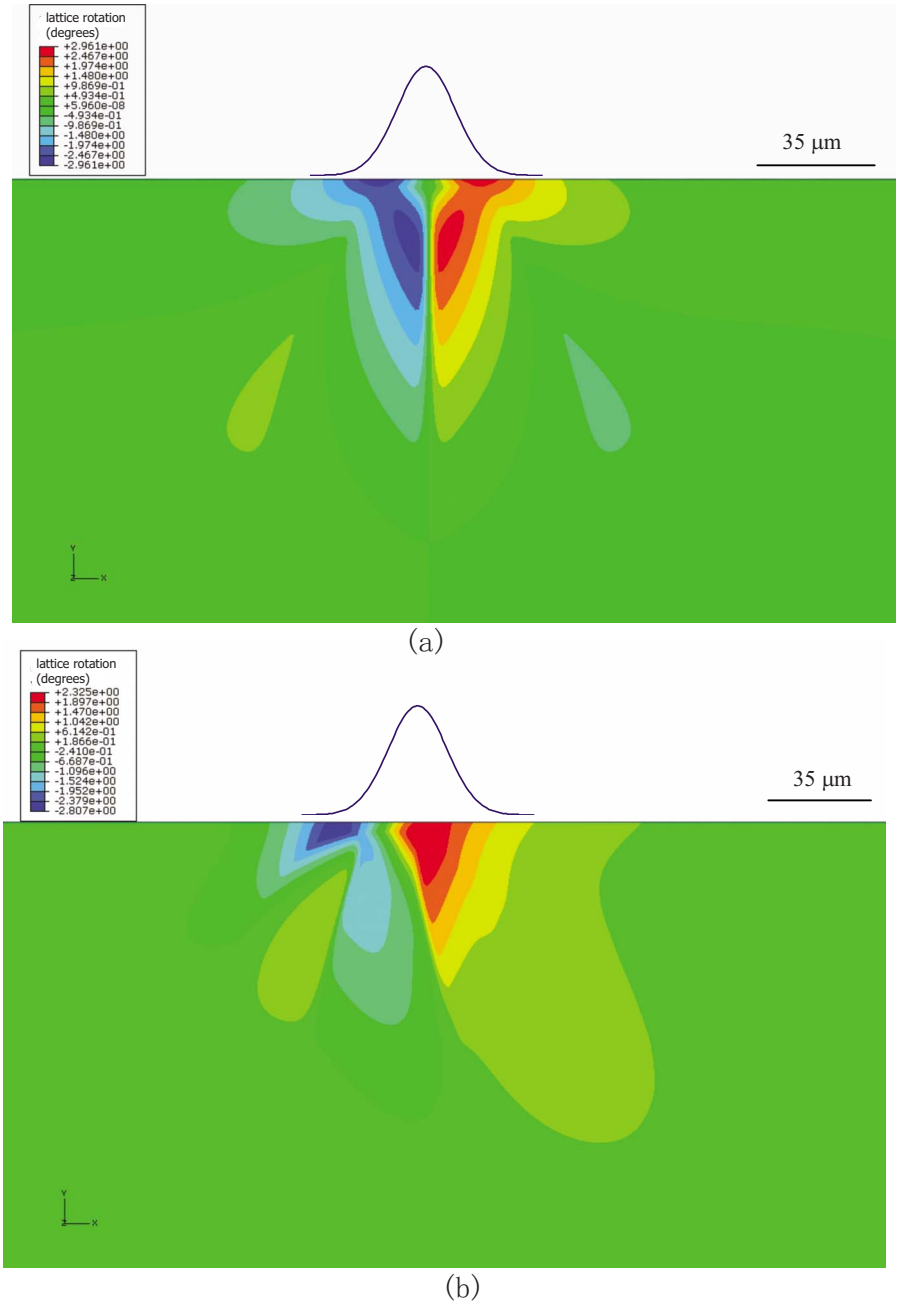

Fig. 8 Lattice deformation contour map by FEM: (*a*) (110) orientation, and (*b*) (1$\bar{1}$4) orientation

case. From the figures it can be noted that response of the (110) crystal is symmetric, and there is asymmetry in the deformation profile of the crystal with (1$\bar{1}$4) orientation. This stems from the asymmetry of the yield surface that leads to the asymmetric response.

5.2 Lattice Rotation Measurements via EBSD and Comparison With Simulation Results. Chen et al. [6] and Wang et al. [18] demonstrated experimentally that plastic deformation due to μLSP will cause the rotation of crystallographic lattice, which can be characterized by means of the EBSD measurements of the attendant lattice rotation. The known undeformed orientation of the crystal serves as the reference state. Therefore it is possible to obtain a mapping of the in-plane rotation of the crystalline lattice induced by the plastic deformation process through comparison of the final crystallographic orientation with the initial one. As a consequence, the angle of in-plane lattice rotation of the crystallographic lattice can be calculated.

Experimental results for the lattice rotation fields of Al (110) and Al (1$\bar{1}$4) on the top surface and in the cross section are shown in Figs. 6 and 7, respectively. Rotation about the shock line center is antisymmetric; the blue region corresponds to counterclockwise rotation (CCW), and the red region corresponds to clockwise rotation (CW). Deformation is largely uniform along the shock line on the treated surface, which indicates that an approximate two-dimensional deformation state is achieved by shocking the single crystal along the (110) direction, which is in good correlation with theoretical predictions of Refs. [12,14]. Deformation of the (110) orientation is approximately symmetric and wider than in the

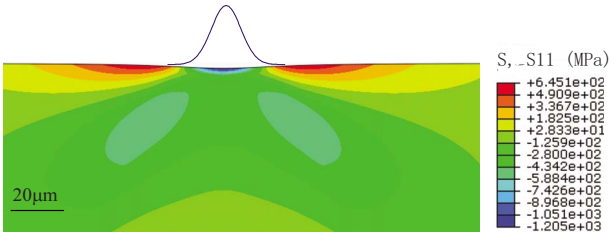

Fig. 9 FEM simulation of residual stress distribution in the (110) case

$(1\bar{1}4)$ case, where the CCW region is about five times smaller than the CW region. The magnitude of lattice rotation is largest between ± 55 μm from the center of the shock line, and it is different for the two cases: it is between ± 4 deg for (110) and ± 2 deg for the $(1\bar{1}4)$ orientation. Similar lattice rotation results, in terms of magnitude, can be observed in EBSD measurement on the cross section (Fig. 7). Here in case of the (110) orientation, the lattice rotates between ± 2.4 deg, which is almost twice the rotation for the $(1\bar{1}4)$ case, which is ± 1.2 deg. Moreover, this result is consistent with the assumption that double slip in the (110) case gives rise to greater rotation of lattice than the single slip case present in the $(1\bar{1}4)$ orientation.

In Fig. 8 the FEM simulation of in-plane lattice rotation of Al for the (110) and $(1\bar{1}4)$ orientations are shown. Simulation results are in good agreement with the experimental findings. It can be seen that in the symmetric (110) orientation case, two main regions of lattice rotation exist. From Fig. 8 it can also be seen that the magnitude of the lattice rotation is larger for the (110) case (which suffers slip on two slip systems) than for the asymmetric $(1\bar{1}4)$ (which has only one slip system active under the Gaussian pressure distribution).

5.3 Stress Distribution. The residual stresses were characterized experimentally based on microdiffraction experiments and analyzed using a method proposed by Ungar et al. [8], which assumes that the deformed crystal is composed of cell walls and soft cell interiors. The cell walls are much harder than cell interiors and therefore the local flow stress is larger in cell walls in comparison to cell interiors. When pressure loading is applied to such a composite model, the cell walls are under compression and cell interiors experience tensile stress. Thus an asymmetric diffraction peak can be decomposed into two symmetric peaks, which belong to "walls" and "interiors," shifted to the left and right from the undeformed diffraction peak, respectively. Measuring the relative difference in angle with respect to the reference undistorted profile will lead to a relative change in lattice spacing Δd, which allows one to estimate the variation in the stress state $\Delta\sigma$ induced by the plastic deformation as $\Delta\sigma=(\Delta d/d)E$, for both cell walls and cell interiors, where E is Young's modulus.

The FEM results of residual stress σ_{11} after unloading is shown at Fig. 9. It can be seen that the stress field is symmetric and a region of compressive residual stress exists in the center region, while a self-equilibrating region of tensile residual stress is present at the peripheries. From the figure it can be seen that when dynamic loading is applied, residual stress distribution trend is much better captured in comparison with previous models [6,18]. Although it has limitations, the numerical models lend much insight into the overall character of the deformation process caused by μLSP, especially with respect to the effects of the anisotropic plastic properties and dynamic material response.

Experimentally, the diffraction profile is measured along a line perpendicular to the shock line with 10 μm between each measurement. From Fig. 10 it can be seen that residual stress estimate is compressive within ± 30 μm from the center of the shock line and tensile in regions 30–60 μm away from the line of shocking to the left and right. Weighted average of the residual stress from the numerical simulation is superimposed in Fig. 10. Weight function is chosen such that it takes into account the fractional contribution of progressively deeper layers to the diffracted intensity [36]. Both numerical values and trend of stress distribution are consistent with experimental measurements, showing that stresses

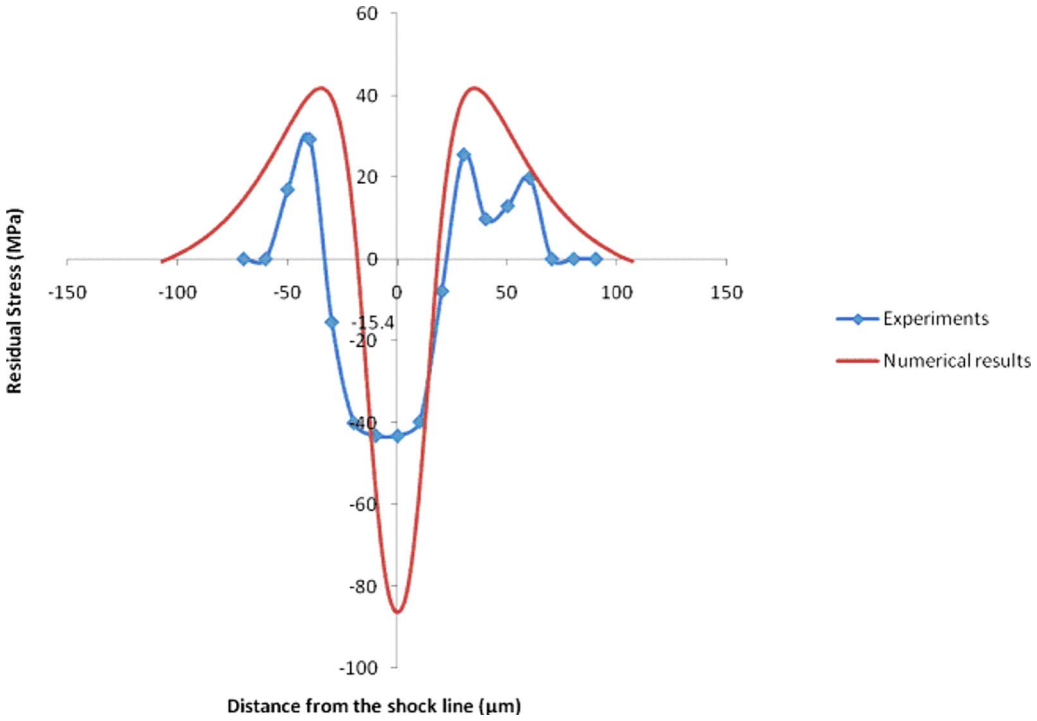

Fig. 10 Residual stress measured via X-ray microdiffraction

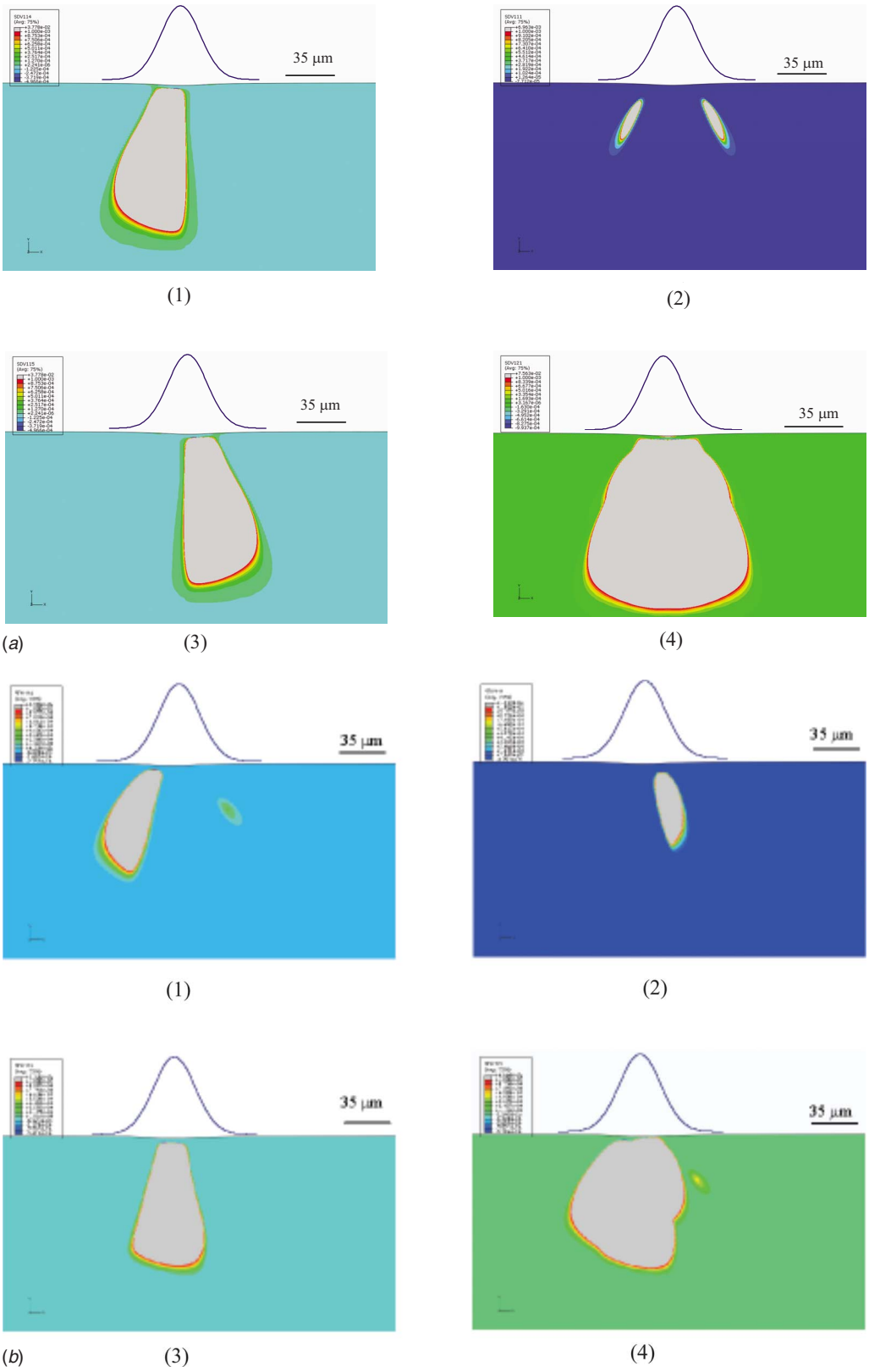

Fig. 11 (*a*) **Shear strain increment in each slip system in the end of the loading step for (110) orientation: (1) increment in slip system *i*; (2) increment in slip system *iii*; (3) increment in slip system *ii*; and (4) total shear strain increment. (*b*) Shear strain increment in each slip system in the end of the loading step for $(1\bar{1}4)$ orientation: (1) increment in slip system *i*; (2) increment in slip system *iii*; (3) increment in slip system *ii*; (4) total shear strain increment**

near to the surface in the region close to the shock line are mostly compressive, which is beneficial for the improvement of fatigue life of microcomponents.

5.4 Wave Propagation and Shear Strain Increments. Propagation of the elastic precursor wave that precedes plastic deformation under μLSP process is analogous to the elastic propagation of waves used in nondestructive evaluation (NDE) for the calculation of ultrasonic field profiles in mildly anisotropic media. This approach considers wave propagation from a finite-sized transducer source, which is equivalent to the compressive surface traction induced by Gaussian pressure distribution. The basis for the NDE is Huygen's principle and retarded potentials based on the existence and properties of the temporal Fourier transformation of Green's function. A closed-form solutions for the point-source in an infinite domain of homogeneous isotropic solid is available [37]. Tverdokhlebov and Rose [38], employing the Helmholtz decomposition, represented Green's function as a sum of three components corresponding to plane wave propagation of quasilongitudinal and two quasitransverse velocities present in the arbitrary anisotropic homogeneous solid. Furthermore, they obtained solution for the point-source problem considering first order weak anisotropy approximation. Numerical implementation is done by Rose et al. [39], by taking into account the finite size transducer source and thus performing analysis beyond plane wave approximation. The results are obtained for centrifugally cast stainless steel (CCSS) compared with experimental findings of Kupperman et al. [40] and Yeong [41].

Numerical integration of Green's function presented by Rose et al. [39] as an output gives elastic wave velocity profiles for quasilongitudinal and two quasitransverse wave modes. These transducer field profiles, in essence, represent strain energy density and from them it can clearly be seen that deformation propagates in the direction of the applied load without little lateral expansion beyond the boundaries of the source. In the case of the μLSP, this effect is observed through the examination of total shear increments, shown in Fig. 11. It appears that plastic deformation occurs predominantly under the Gaussian pressure load for both (110) and $(1\bar{1}4)$ crystal orientations. In addition, another important consequence of anisotropy should be noted. The wavefront normal vector does not coincide with the wave velocity vector for an anisotropic medium. This leads to the skewing of the direction of the strain energy density propagation in the direction of large phase velocity, resulting in the asymmetric material response. Comparing total shear increments shown in Fig. 11 and yield loci in Figs. 4(*a*) and 4(*b*), it can be seen that plastic deformation propagates in the direction of the longitudinal axis of symmetry of yield loci showing that symmetric and asymmetric yield surfaces produce symmetric and asymmetric plastic deformations.

Plastic deformation in the simulation is represented through shear strains. It is of interest to closely examine shear strain increments for each slip system as well as total shear strain increment, which are shown on Figs. 11(*a*) and 11(*b*) for both the (110) and the $(1\bar{1}4)$ cases. From Fig. 11(*a*) it can be seen that for the (110) case, shear increments associated with slips *i* and *iii* are antisymmetric with respect to the center line of the Gaussian pressure distribution, whereas the shear increment on slip system *ii* is symmetric. On the other hand for the $(1\bar{1}4)$ orientation (see Fig. 11(*b*)), the magnitude and distribution of shear increments on the three effective in-plane slip system are larger than on the left side as seen on Fig. 11. Thus, the symmetric yield locus gives rise to a symmetric displacement field for the (110) case and the asymmetric one is associated with asymmetric displacement field for the $(1\bar{1}4)$ case. Furthermore deformation propagates deeper into the material in the double slip case (110) orientation of the crystal than in the case of the single slip $(1\bar{1}4)$ case.

6 Conclusion

Dynamic material response under microscale laser shock peening and the comparison between two different orientations of aluminum single crystal—one symmetric and one asymmetric—is presented in this paper. In the case of the double slip symmetric case plastic deformation caused by each slip system adds to the total deformation as characterized by the lattice rotations, which suggests that deformation in the symmetric orientation will be greater than in the asymmetric case. A numerical model is established for more detailed investigation of the μLSP process and compared with experiments. Both effects of anisotropy with wave propagation and dynamic material response have been considered in the numerical analysis. Experimental measurement of the lattice rotation via EBSD in the double slip case lattice rotation is about twice as large as in the single slip, when effects of anisotropy are solely considered, which is consistent with the analytic work. Residual stress is characterized using X-ray microdiffraction and compared with numerical results.

Acknowledgment

This work is supported by National Science Foundation under Grant No. DMII-0500239. Dr. Jean Jordan Sweet of IBM Watson Research Center provided help with usage of X-ray microdiffraction equipment at the National Synchrotron Light Source at Brookhaven National Laboratory. This work has used the shared experimental facilities that are supported primarily by the MRSEC Program of the National Science Foundation under Award No. DMR-0213574 by the New York State Office of Science, Technology and Academic Research (NYSTAR). Dr. Paul van der Wilt generously assisted during EBSD measurements.

References

[1] Clauer, A. H., and Holbrook, J. H., 1981, "Effects of Laser Induced Shock Waves on Metals," *Shock Waves and High Strain Phenomena in Metals-Concepts and Applications*, New York, pp. 675–702.
[2] Clauer, A. H., and Lahrman, D. F., 2001, "Laser Shock Processing as a Surface Enhancement Process," Key Eng. Mater., **197**, pp. 121–142.
[3] Fabbro, R., Fournier, J., Ballard, P., Devaux, D., and Virmont, J., 1990, "Physical Study of Laser-Produced Plasma in Confined Geometry," J. Appl. Phys., **68**(2), pp. 775–784.
[4] Hammersley, G., Hackel, L. A., and Harris, F., 2000, "Surface Prestressing to Improve Fatigue Strength of Components by Laser Shot Peening," Opt. Lasers Eng., **34**(4–6), pp. 327–337.
[5] Zhang, W., and Yao, Y. L., 2002, "Microscale Laser Shock Processing of Metallic Components," ASME J. Sol. Energy Eng., **124**, pp. 369–378.
[6] Chen, H. Q., Kysar, J. W., and Yao, Y. L., 2004, "Characterization of Plastic Deformation Induced by Microscale Laser Shock Peening," ASME J. Appl. Mech., **71**(5), pp. 713–723.
[7] Chen, H. Q., Yao, Y. L., and Kysar, J. W., 2004, "Spatially Resolved Characterization of Residual Stress Induced by Micro Scale Laser Shock Peening," ASME J. Manuf. Sci. Eng., **126**(2), pp. 226–236.
[8] Ungar, T., Mughrabi, H., Ronnpagel, D., and Wilkens, M., 1984, "X-Ray Line-Broadening Study of the Dislocation Cell Structure in Deformed [001]-Orientated Copper Single-Crystals," Acta Metall., **32**(3), pp. 333–342.
[9] Hill, R., 1998, *The Mathematical Theory of Plasticity* (Oxford Engineering Science Series), Clarendon, Oxford/Oxford University Press, New York.
[10] Hencky, H., 1923, "Concerning the on Static Dependent Equilibrium of Plastic Material," Z. Angew. Math. Mech., **3**, pp. 241–251.
[11] Prandtl, L., 1923, "Anwendungsbeispiele Zu Einem Henckyschen Salt Über Das Plastische Gleichgewicht," Z. Angew. Math. Mech., **3**, pp. 401–406.
[12] Rice, J. R., 1973, "Plane Strain Slip Line Theory for Anisotropic Rigid-Plastic Materials," J. Mech. Phys. Solids, **21**(2), pp. 63–74.
[13] Booker, J. R., and Davis, E. H., 1972, "General Treatment of Plastic Anisotropy Under Conditions of Plane Strain," J. Mech. Phys. Solids, **20**(4), pp. 239–250.
[14] Rice, J. R., 1987, "Tensile Crack Tip Fields in Elastic Ideally Plastic Crystals," Mech. Mater., **6**(4), pp. 317–335.
[15] Drugan, W. J., 2001, "Asymptotic Solutions for Tensile Crack Tip Fields Without Kink-Type Shear Bands in Elastic-Ideally Plastic Single Crystals," J. Mech. Phys. Solids, **49**(9), pp. 2155–2176.
[16] Kysar, J. W., and Briant, C. L., 2002, "Crack Tip Deformation Fields in Ductile Single Crystals," Acta Mater., **50**(9), pp. 2367–2380.
[17] Kysar, J. W., Gan, Y. X., and Mendez-Arzuza, G., 2005, "Cylindrical Void in a Rigid-Ideally Plastic Single Crystal. Part I: Anisotropic Slip Line Theory Solution for Face-Centered Cubic Crystals," Int. J. Plast., **21**(8), pp. 1481–1520.
[18] Wang, Y., Kysar, J. W., and Yao, Y. L., 2008, "Analytical Solution of Aniso-

tropic Plastic Deformation Induced by Micro-Scale Laser Shock Peening," Mech. Mater., **40**(3), pp. 100–114.
[19] Fox, J. A., 1974, "Effect of Water and Paint Coatings on Laser-Irradiated Targets," Appl. Phys. Lett., **24**(10), pp. 461–464.
[20] Crone, W. C., Shield, T. W., Creuziger, A., and Henneman, B., 2004, "Orientation Dependence of the Plastic Slip Near Notches in Ductile FCC Single Crystals," J. Mech. Phys. Solids, **52**(1), pp. 85–112.
[21] SPEC X-Ray Diffraction Software, Certified Scientific Software, Cambridge, MA.
[22] Fan, Y., Wang, Y., Vukelic, S., and Yao, Y. L., 2005, "Wave-Solid Interactions in Laser-Shock-Induced Deformation Processes," J. Appl. Phys., **98**(10), pp. 104904–104904-11.
[23] Peyre, P., Sollier, A., Chaieb, I., Berthe, L., Bartnicki, E., Braham, C., and Fabbro, R., 2003, "FEM Simulation of Residual Stresses Induced by Laser Peening," Eur. Phys. J. Appl. Phys., **23**(2), pp. 83–88.
[24] Johnson, J. N., 1972, "Calculation of Plane-Wave Propagation in Anisotropic Elastic-Plastic Solids," J. Appl. Phys., **43**(5), pp. 2074–2082.
[25] Nemat-Nasser, S., Okinaka, T., Nesterenko, V., and Liu, M. Q., 1998, "Dynamic Void Collapse in Crystals: Computational Modelling and Experiments," Philos. Mag. A, **78**(5), pp. 1151–1174.
[26] Asaro, R. J., 1983, "Micromechanics of Crystals and Polycrystals," Adv. Appl. Mech., **23**, pp. 1–115.
[27] Huang, Y., 1991, "A User-Material Subroutine Incorporating Single Crystal Plasticity in the ABAQUS Finite Element Program," Division of Applied Sciences, Harvard University, Mech. Report No. 178.
[28] Kysar, J. W., 1997, "Addendum to a User-Material Subroutine Incorporating Single Crystal Plasticity in the ABAQUS Finite Element Program," Division of Applied Sciences, Harvard University, Mech. Report No. 178.
[29] ABAQUS Theory Manual, 1997, Hibbitt, Karlsson and Sorensen, Inc.
[30] Zienkiewicz, O. C., Taylor, R. L., Zhu, J. Z., and Knovel, 2005.
[31] Schmid, E., 1931, "Articles on the Physics and Metallography of Magnesiums," Z. Elektrochem. Angew. Phys. Chem., **37**, pp. 447–459.
[32] Hutchinson, J. W., 1976, "Bounds and Self-Consistent Estimates for Creep of Polycrystalline Materials," Proc. R. Soc. London, Ser. A, **348**(1652), pp. 101–127.
[33] Bassani, J. L., and Wu, T. Y., 1991, "Latent Hardening in Single-Crystals 2. Analytical Characterization and Predictions," Proc. R. Soc. London, Ser. A, **435**(1893), pp. 21–41.
[34] Cuitino, A. M., and Ortiz, M., 1993, "Computational Modeling of Single-Crystals," Modell. Simul. Mater. Sci. Eng., **1**(3), pp. 225–263.
[35] Peirce, D., Asaro, R. J., and Needleman, A., 1983, "Material Rate Dependence and Localized Deformation in Crystalline Solids," Acta Metall., **31**(12), pp. 1951–1976.
[36] Noyan, I. C., and Cohen, J. B., 1987, *Residual Stress: Measurement by Diffraction and Interpretation, Materials Research and Engineering*, Springer-Verlag, New York.
[37] Achenbach, J. D., 1975, *Wave Propagation in Elastic Solids* (North-Holland Series in Applied Mathematics and Mechanics), North-Holland, Elsevier, Amsterdam/New York.
[38] Tverdokhlebov, A., and Rose, J., 1988, "On Green-Functions for Elastic-Waves in Anisotropic Media," J. Acoust. Soc. Am., **83**(1), pp. 118–121.
[39] Rose, J. L., Balasubramaniam, K., and Tverdokhlebov, A., 1989, "A Numerical Integration Green's Function Model for Ultrasonic Field Profiles in Mildly Anisotropic Media," J. Nondestruct. Eval., **8**(3), pp. 165–179.
[40] Kupperman, D. S., Reimann, K. J., and Abregolopez, J., 1987, "Ultrasonic NDE of Cast Stainless-Steel," NDT Int., **20**(3), pp. 145–152.
[41] Yeong, P. Y., 1987, "Ultrasonic Characterization of Centrifugally Cast Stainless Steel," Ph.D. thesis, Palo Alto, CA.